

No

Paper to be presented at  
AIAA 3rd Aerodynamic Testing Conference  
San Francisco, California, April 8-10, 1968

A TECHNIQUE FOR DETERMINING THE SPATIAL DISTRIBUTION OF  
RELATIVE RADIANT INTENSITY IN SHOCK LAYERS OVER BODIES  
AT ANGLE OF ATTACK AT HYPERSONIC VELOCITIES

By Robert M. Reynolds\*

National Aeronautics and Space Administration  
Ames Research Center  
Moffett Field, California 94035

Described is a technique for obtaining experimentally, in a ballistic range, a complete mapping of the spatial distribution of the relative intensities of radiating gases over the front surfaces of models at angle of attack. Results are presented for four different models at velocities between 5.5 and 6.8 km/sec and at angles of attack up to 36°. All models were launched into a 50% CO<sub>2</sub> - 50% N<sub>2</sub> gas mixture at ambient pressures between 5 and 60 torr.

INTRODUCTION

Among the problems of interest in the field of radiative heat transfer to bodies entering planetary atmospheres is the spatial distribution of the radiation in the shock layer. The design of the heat shield requires knowledge of the heating rates to areas other than the stagnation region, particularly since these areas generally comprise the largest part of the heat shield. The problem is difficult when the effects of angle of attack must be considered. The shock layers of interest, frequently subsonic, are no longer axially symmetric, so that, for other than the simplest of shapes, a reliable analytical prediction of the shock layer radiation may be beyond the capabilities of current theory.

Experimental data relating to this problem are meager. Givens, Canning, and Bailey<sup>1</sup> used an image-dissector technique to obtain radial

\*Research Scientist, Hypersonic Free-Flight, Vehicle Environment Division

STTI Prices -  
(HC) - 3.00

FACILITY FORM 602	<b>N 68-34873</b>	
	(ACCESSION NUMBER)	(THRU)
	21	1
	(PAGES)	(CODE)
TMX-61224	33	
(NASA CR OR TMX OR AD NUMBER)	(CATEGORY)	

distributions of relative intensity for spherical-nosed bodies at zero angle of attack. Walters<sup>2</sup> has reported measurements of the total radiation from the gas cap of Apollo models as a function of angle of attack. Dyner and Reinecke<sup>3</sup> employed broad-band radiometers viewing three model shapes head-on to measure the total over-the-body equilibrium heating load as a function of angle of attack, and, in addition, used a blunted-cone model instrumented with fiber optics to determine the radial distribution of radiative heating at zero angle of attack. None of these references reports spatial distributions of radiative heating for models at angle of attack.

The purpose of the present paper is to describe a technique used in the Hypervelocity Free-Flight Radiation Facility at Ames Research Center for mapping the relative radiative distribution over models at angle of attack, providing much greater detail than any of the methods previously reported. The technique is not difficult to use, and provides additional data simultaneously with and supplementary to more conventional broad- and narrow-band radiometer observations. The data were obtained concurrently in tests relating to studies of the feasibility of measuring the composition of the Martian atmosphere by means of shock-layer spectrometry instrumentation aboard an entering probe, both for spherical-nosed shapes<sup>4</sup> and a blunted-cone shape proposed by the Jet Propulsion Laboratory for the Voyager vehicle<sup>5</sup>.

## EXPERIMENTAL TECHNIQUES

### Facility

All data reported herein were obtained in the Ames Hypervelocity Free-Flight Radiation Facility, shown schematically in Fig. 1. Not shown, but a part of the facility nevertheless, are a shock-tube driver and nozzle which, for certain tests, provide a counter current gas stream. The models are launched from a caliber 3.81 cm, deformable-piston, light-gas gun.

As the models fly through the test section, which for these tests was filled with a 50 % CO<sub>2</sub>-50 % N<sub>2</sub> gas mixture, they are observed at four spark-shadowgraph stations spaced at 1.83 meter intervals along its length. These shadowgraphs, together with the time intervals between stations (measured with electronic chronographs), provide the model velocity and angle-of-attack history. The free-stream pressure (selected in these tests to obtain thermodynamic equilibrium in the shock layer) and temperature of the gas mixture are measured just prior to launching of the model.

#### Models

All models used in these tests were made of Delrin, n(CHOH), which experience has shown does not produce significant ablation-products radiation in the spectral range of interest<sup>6</sup>. Four different model configurations were studied, two being simple spherical noses and two being moderately-blunted rounded-nosed 60° cones. The latter are models of a proposed Voyager configuration for use in entering the Martian atmosphere. Only one model, the last blunted-cone model, required the use of a 4-piece Lexan sabot to facilitate its launching. Sketches of the models, together with a listing of the test conditions, appear on subsequent figures of the report, adjacent to the data to which they pertain.

#### Radiometers

Although the data are not reported herein, it may be of interest to note the complete instrumentation used for these tests. Four broadband radiometers (S-5 spectral response), one pair mounted orthogonally at each of two range stations, observed the model shock layer radiation in side view<sup>7</sup>. Also viewing the model gas cap from the side were 14 monochrometers, covering the spectral range from 0.346 to 0.975 microns, mounted together and aligned in nearly the same direction. In addition, the spectra emitted from the shock layers about the spherical-nosed models were recorded with a scanning spectrometer<sup>9</sup>. All radiometers were calibrated against a standard tungsten source to determine their absolute

radiant sensitivity, and their output signals on oscilloscopes were recorded photographically. It is planned to relate these radiometric data to the spatial radiant intensity distributions found by the method subsequently described herein.

#### Image Converter Camera

The luminous flow about the models was recorded in near head-on view (via an angled mirror, sighting approx.  $4^{\circ}$  off-axis) by a TRW Model 1-D image converter camera.<sup>10</sup> This model has an S-11 spectral response, and was operated in a framing mode which provides 3 frames at 1 microsecond intervals, with an exposure time of 200 nanoseconds. A 50.8cm focal length Aero Ektar lens was used as an objective (providing magnification = .24) to focus the image of an object located at the third test station on the camera photocathode. The camera trigger was taken from the spark source for the shadowgraphs of the third station, so that both of these shadowgraphs and the image converter camera picture were obtained simultaneously.

#### Analysis of Image Converter Camera Pictures

A Joyce-Loebl recording microdensitometer fitted with a Technical Operations Isodensitracer was used in analyzing the image converter camera pictures of the self-luminous gas caps on the models. A schematic of the microdensitometer, indicating most of the variables at the control of the operator, is shown in Fig. 2. Note that the instrument has a double-beam light system, in which separate beams from a single light source are switched alternately to a single photo-multiplier. This makes the instrument independent of line voltage and aging of the light source, permitting excellent reproducibility of records. When the two beams are of different intensity, a signal is produced by the photomultiplier, which, after amplification, causes the servo motor to move the grey wedge in the reference beam until the intensity difference becomes zero. Thus, the system is continuously null balancing, and the position of the grey wedge is directly related to the film density of the specimen.

In normal use, the microdensitometer will scan along a single line and present optical density as a function of displacement along the scan. The Isodensitracer attachment permits automatic, consecutive, parallel scanning of a multitude of traces, measuring the optical density at all points along each trace and plotting the values as a quantitative, two-dimensional density map of the scanned area. The manner in which this is accomplished is illustrated in Fig. 3. A solenoid-driven pen, controlled by a commutator in the grey wedge drive system, prints out a code of dashes, dots, and blanks. As long as the film density remains within the boundaries dictated by the combination of grey wedge and commutator used, a given code will be printed out. The sequence of code changes is orderly with increasing film density, and reverses direction, or order, as film density decreases. Thus, by noting the sequence of code changes with displacement along the scan, the normal single scan of the microdensitometer may be reconstructed, albeit with a little less detail. Of particular advantage is the fact that once the two-dimensional density map of the scanned area has been recorded the choice of direction and location of a "particular" scan becomes unlimited, a choice which is virtually impossible when working with the film transparency alone.

All that remains, then, is a means of relating the film optical density to the intensity of the light source which exposes the film. How this is accomplished is illustrated in Fig. 4. After the film has been exposed to the luminous flow field on the face of the models, and prior to its development, a strip of the film is exposed to an incandescent light source, for a time,  $t$ , through a photographic step wedge having a series of steps of known transmission,  $T_n$ , and corresponding optical density  $D_n$ . Then, given the definition that optical density,  $D$ , equals  $\log_{10}$  of the reciprocal of the transmission, it is readily seen (Fig. 4a) that the relative exposure of a given step on the exposed film is related logarithmically to the optical density of the corresponding step of the photographic step wedge. After development of the film, the densities of

the steps are measured with the microdensitometer, and are plotted against the corresponding densities of the steps of the photographic step wedge (Fig. 4b), forming the film characteristic (Hurter-Driffield) curve. The Isodensitrace is then made of the gas cap film image, using exactly the same microdensitometer settings so as not to shift the zero density level, and plots of film density as a function of some coordinate are reconstructed (Fig. 4c). Each density point on this plot corresponds to a particular value of  $\log_{10}$  of the relative exposure (Fig. 4b). Then, by subtracting logarithms, the  $E_0$  term (exposure for 100% transmission) is eliminated, leaving only the logarithm of the relative exposure of any point on the film compared to the point of maximum exposure. Since all points of the film image are exposed for the same time,  $t$ , values of relative exposure must equal values of relative intensity of the radiating source.

### Results

Fig. 5 presents Isodensitraces, along the corresponding shadowgraphs and image-converter camera pictures, for the spherical-nosed models. These traces, and those shown subsequently, were made using a geometrical magnification of the film image of 20 times. An effective primary slit of 100 microns square was used; thus approximately 0.01% of the film image was scanned at any instant. Various grey wedge-commutator combinations were tried initially, but best results were generally obtained with those giving density-step increments of 0.04 or 0.06. The horizontal lines apparent in the image converter camera picture, and reflected in the Isodensitraces, are inherent to the camera, and are caused by a biasing grid in the image converter tube. Their disturbance is local and can generally be faired out of the density plots if the trace being considered crosses a biasing grid line. The model diameter, developed as a dark circle on the Isodensitrace, was calculated knowing the optical magnification of the camera-lens system and the geometrical magnification of the Isodensitrace relative to the film image. Since the image converter camera pictures contain no reference system, other than the approximately horizontal grid lines, it is necessary to locate the model boundary by matching it to the isodensity contours. For the small angles of attack ( $\alpha$ ) and yaw ( $\beta$ )

shown, the difference between a circular section of the model and its elliptic trace in the y-z plane is not discernible. Also, the effect of the small ( $4^\circ$ ) off-axis angle of the image-converter-camera mirror has been neglected.

In regard to the image converter camera pictures, it has been shown <sup>11, 12</sup> that the CN violet band system is the most prominent spectral radiator in the gas caps of models flying at the test velocities,  $V_\infty$ , into  $\text{CO}_2 - \text{N}_2$  gas mixtures at the test pressures,  $p_\infty$ . The S-11 response of the image converter camera tube peaks over the wavelengths (approx. 0.38 - 0.42 microns) of the CN violet system, so that it is estimated that approximately 85% of the total radiation from the model shock layers is observed.

The shadowgraph photos have been cropped so that their edges are parallel to the test section reference axis.

The film density and relative intensity distributions for the spherical-nosed bodies of different bluntness are compared in Fig. 6. Both of these traces were made along horizontal lines through the estimated center of the model in order to avoid the grid-line disturbances. It should be noted here that at the time the Isodensitraces are made, a single trace is made with the microdensitometer in the normal continuous-writing mode, along a line crossing the region of maximum film density and corresponding to one of the coded lines on the Isodensitrace. This serves to accurately establish the values of the peak densities (Fig. 6a), and provides a proof of the accuracy of the coded line. As would be anticipated, the relative intensity curves of Fig. 6(b) appear reasonably symmetric, with the curve for the model of  $r_n/D = .67$  not as broad as that for an  $r_n/D = 1.44$ . This is because the sonic point of the flow at the model surface is at a lesser  $r/R$  for the model with smaller nose radius, compared with that for the model with  $r/D = 1.44$ . (Author's note: In the final form, it is planned to compare at this point at least one of these curves with a theoretical curve).

Figures 7 and 8 present the results for the blunted-cone model in a format identical to those previously discussed. The film density distributions (Fig. 8(a)) were made along the corresponding traces shown in Fig. 7, i.e., along surface elements at a roll angle,  $\phi$ , with reference to the vertical test section axis. Note that the trace in Fig. 7(a) crosses a bias grid of the image converter camera picture, as reflected in the fairing of the corresponding density distribution in Fig. 8(a). The data of Fig. 7(b) did not present this problem, but the corresponding density trace (Fig. 8(a)) required, on the leeward side, the fairing of the density curve through the centroid of the areas between  $\frac{r}{R} = .31$  to  $.98$ . Comparison of the relative intensity curves for these two launchings of identical models (Fig. 8(b)) shows good repeatability of the data, with the lower relative intensities on the leeward side of the latter launching consistent with its higher resultant angle of attack.

The results for a sabot-launched blunted cone (with non-dimensionalized face coordinates identical to those of the previously discussed models), flying at a large resultant angle of attack, are presented in Figures 9 and 10. The grid system defining the model surface, and overlaying the isodensitrace (Fig. 9), was calculated from the measured values of  $\rho$  and  $\tau$  from the shadowgraphs, the known variation of model radius with distance from the model base, and the optical and geometric magnification factors. The calculated model surface grid matches the isodensity contours quite reasonably. While the relative intensity distribution has been calculated only along the meridian of flow symmetry (Fig. 10(b)), it is readily seen that a complete mapping of relative intensity as a function of model surface coordinate is feasible. Calculating a reliable theoretical distribution for comparison is another problem.

### Conclusions

The results presented herein, while at this point minimally compared with theory, (Note: assuming only one theory curve will be available) appear reasonable and seem to demonstrate the feasibility of experimentally defining in rather complete detail the relative radiative intensity distributions from luminous shock layers, including those of bodies at large angles of attack. It has been shown that the relative intensity distributions measured for spherical-nosed models by this technique reflect the difference in nose radius, and are related in an appropriate sense. Also, it has been shown for the blunted-cone Voyager shape that for nearly equal test conditions the derived relative intensity distributions were nearly identical, even reflecting in the proper sense the difference in the resultant angles of attack of the two models. Further, a mapping of the spatial distribution of relative radiant intensities in the shock layers of the Voyager shape at a high angle of attack has been shown, which, when combined with a computed absolute value for the radiant intensity at the stagnation region, would give absolute spatial radiative distributions not readily available by any other means. This latter, then, is the signal advantage of the technique-i.e., measurements can be made available of the distribution of radiance in the shock layers of configurations, and at attitudes, for which reliable theoretical solutions do not exist.

Factors to be considered in future work might include the following:

- (1) Find some means of eliminating the bias grid distortion and establishing a coordinate reference system on the image converter camera picture.
- (2) Along with tests to prove that the photographic step wedges are neutral, i.e., not wavelength dependent, devise a means of exposing them onto the film record via the same mirror-lens-camera path taken by the radiation from the model shock layers, so as to account for any non-linearity in the response of the over-all camera system.

(3) Relate the broad- and narrow-bandpass radiometric data to the integrated radiant intensity over that portion of the gas cap which can be seen by the radiometers.

References

1. Givens, John J., Canning, Thomas N., and Bailey, Harry E., "Measurements of spatial distribution of shock-layer radiation for blunt bodies at hypersonic speeds," NASA TM X-852 (January, 1964). (Confidential).
2. Walters, Edward E., "Free-flight measurements of radiative heating to the front face of the Apollo reentry capsule as a function of angle of attack," NASA TM X-851 (February, 1964). (Confidential).
3. Dyner, H. B., and Reinecke, W. G., "Simulation of total equilibrium shock layer radiation for three typical entry body shapes" AIAA Paper No. 67-324 (April, 1967).
4. Whiting, E. E., "Determination of Mars atmospheric composition shock-layer radiometry during a probe experiment", AIAA Paper No. 67-293 (April, 1967).
5. Wolf, Fred, and Spiegel, Joseph M., "Status of basic shock-layer radiation information for inner-planet atmospheric entry", Jnl. Spacecraft and Rockets, 4, No. 9, 1166-1173 (September, 1967).
6. Reis, V. H., "Oscillator strengths for the N<sub>2</sub> second positive and N<sub>2</sub><sup>+</sup> first negative systems from observations of shock layers about hypersonic projectiles," J. Quant. Spectr. Radiative Transfer 4. 783-792 (1964).
7. Compton, Dale L., and Cooper, David M., "Measurements of radiative heating on sharp cones", AIAA Jnl., Vol. 3, No. 1, (January, 1965).
8. Craig, Roger A., and Davy, William C., "Absolute radiometers for use in ballistic ranges and shock tubes". (Paper in preparation).
9. Whiting, E. E., "A new four-channel scanning spectrometer for ballistic-range radiometry", Proceedings of IEEE Second International Congress on Instrumentation in Aerospace Simulation Facilities, Stanford Univ., (August, 1966).
10. "Characteristics of the TRW Image Converter Cameras", TRW Instruments, El Segundo, California.
11. James, C.S., "Experimental study of radiative transport from hot gases simulating in composition the atmospheres of Mars and Venus," AIAA Paper No. 63-455 (December, 1963).
12. Arnold, J. O., Reis, V.H., and Woodward, H.T., "Studies of shock-layer radiation of bodies entering planetary atmospheres," AIAA J. 3, 2019-2025 (November, 1965).

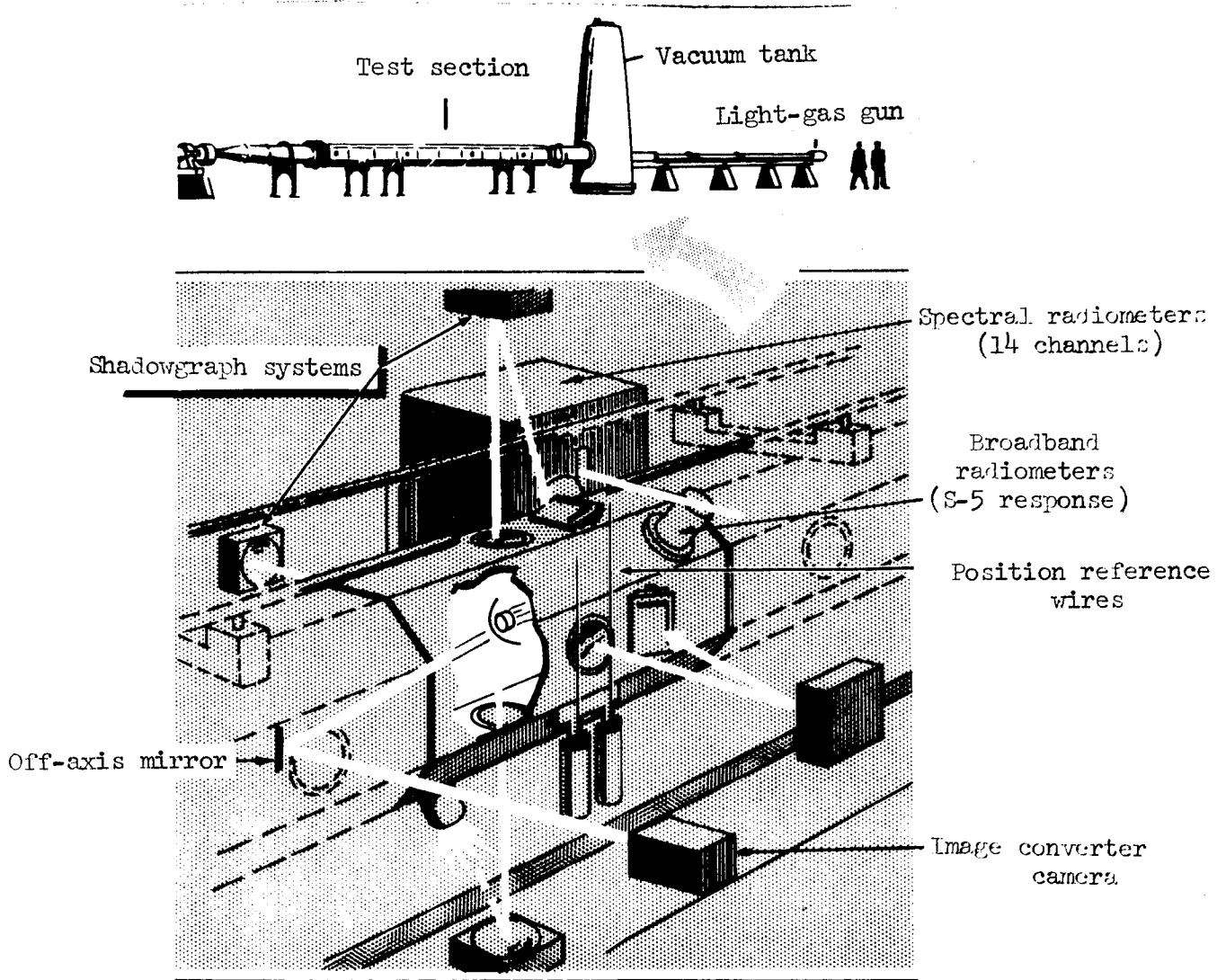


Figure /.- Schematic drawing of hypervelocity free-flight radiation facility.

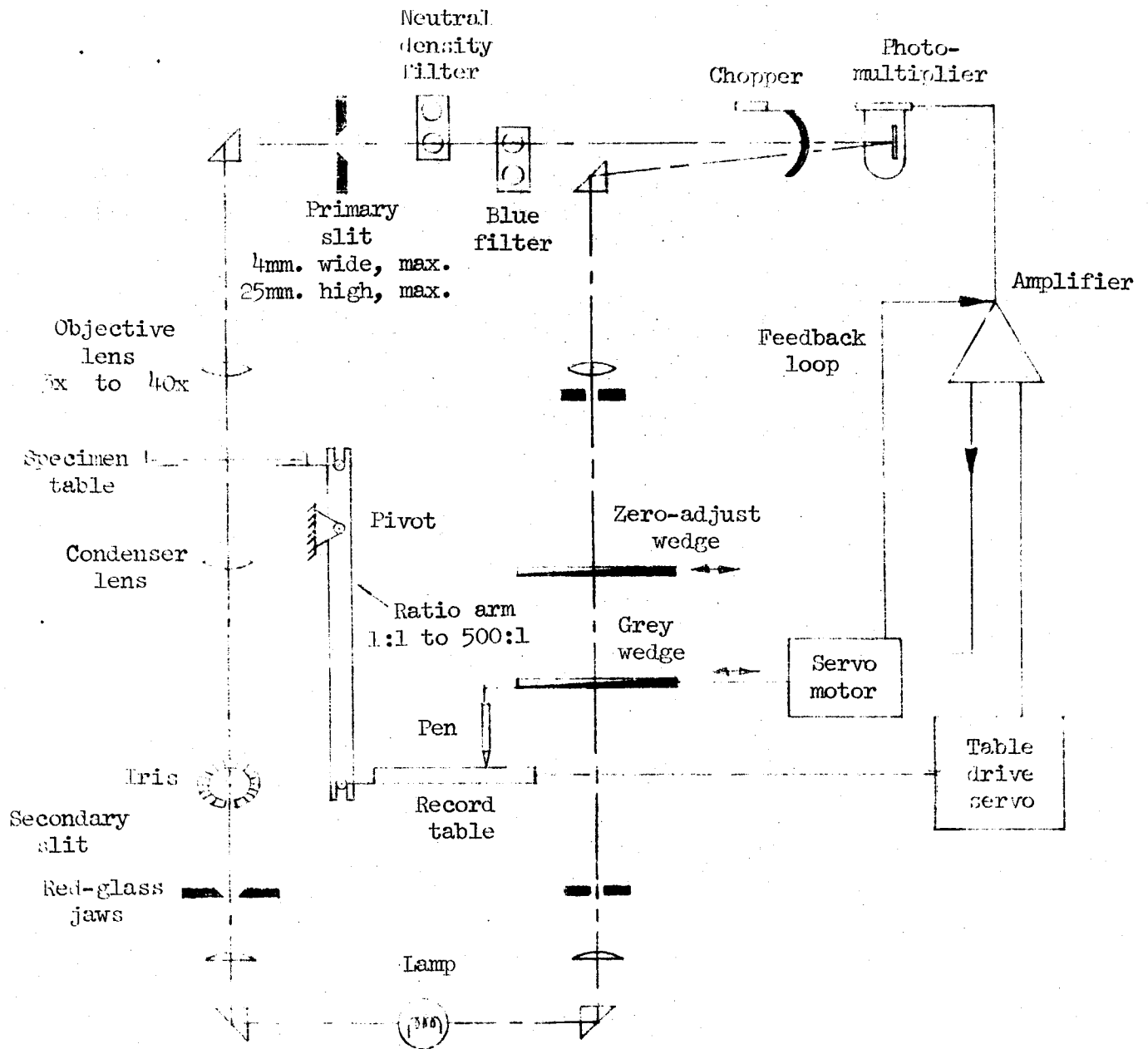


Figure 2.- Microdensitometer schematic.

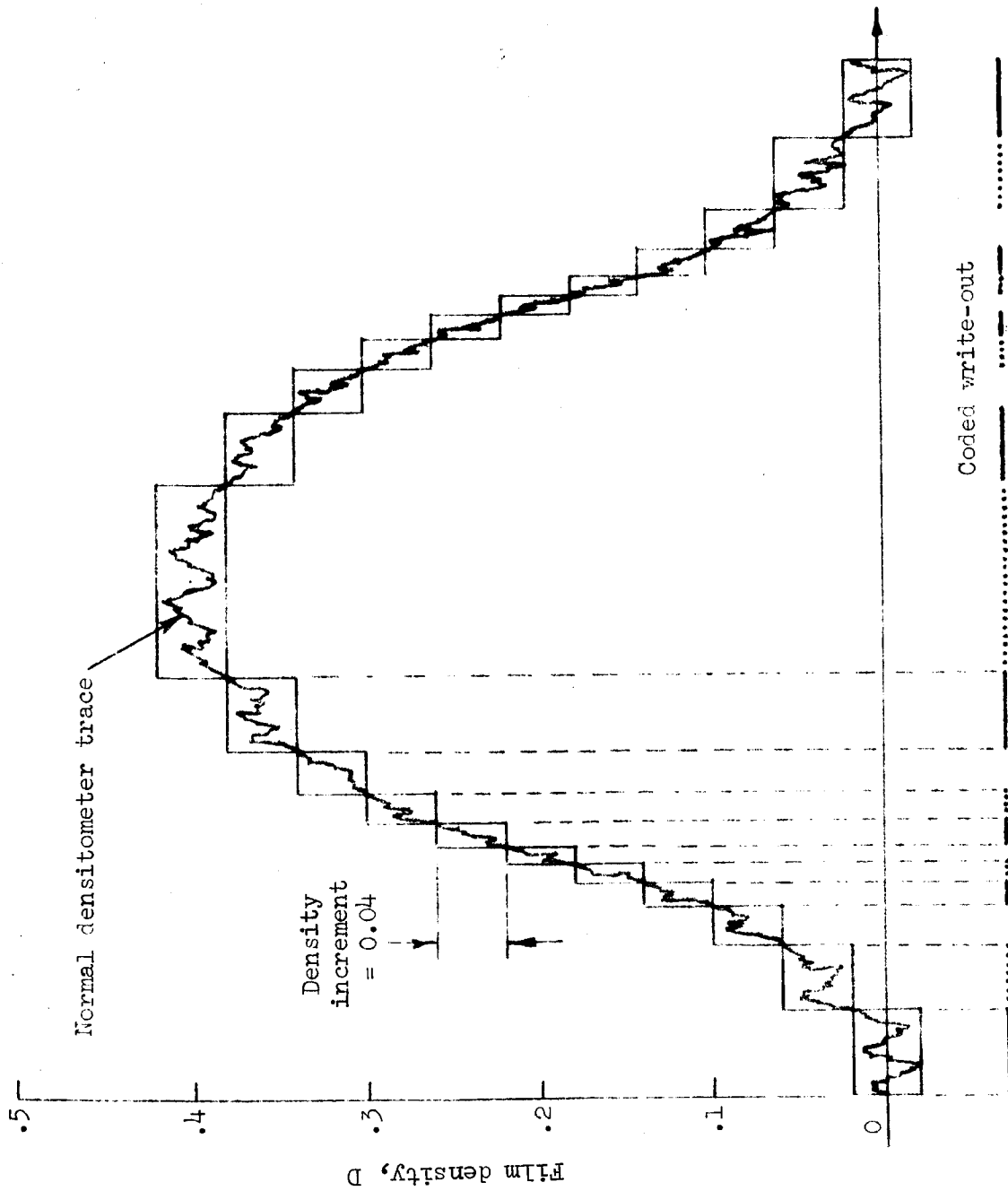
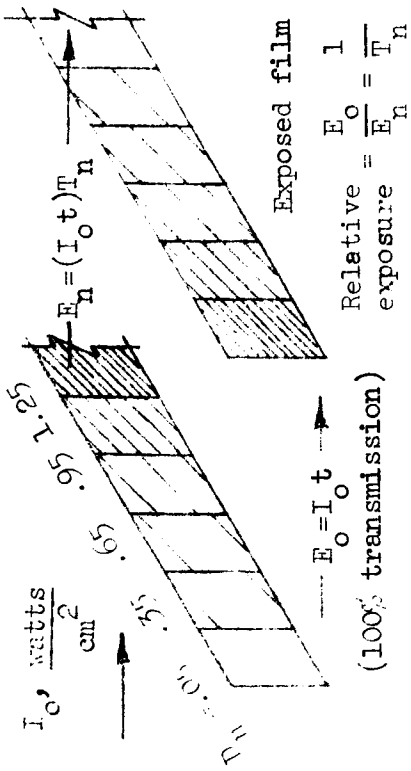


Figure 3.- Coding method for Isodensitracer write-out.

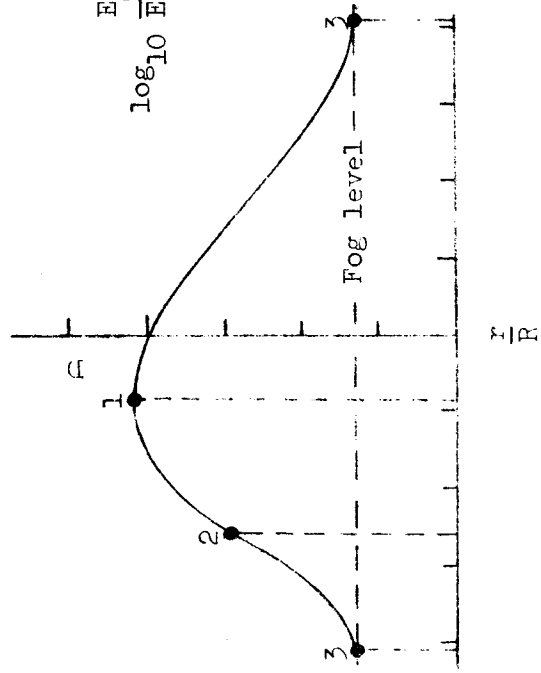
Kodak 1a wedge



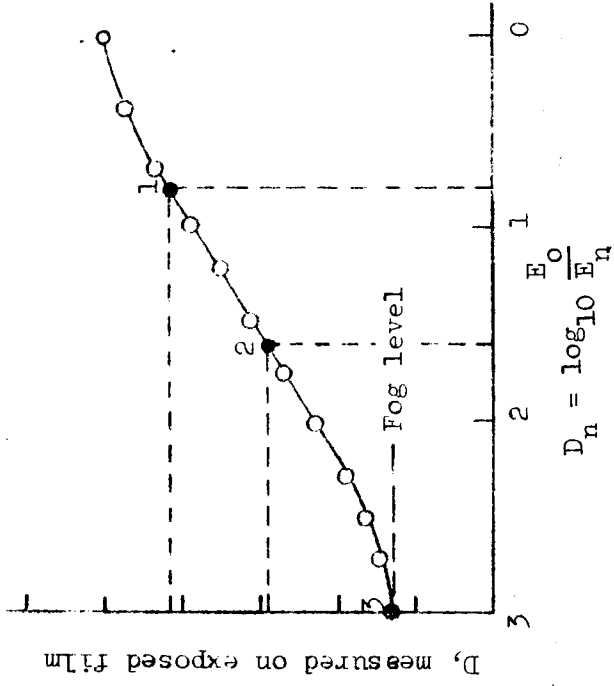
$$D = \log_{10} \frac{1}{T}$$

$$\log_{10} \frac{E_0}{E_n} = D_n$$

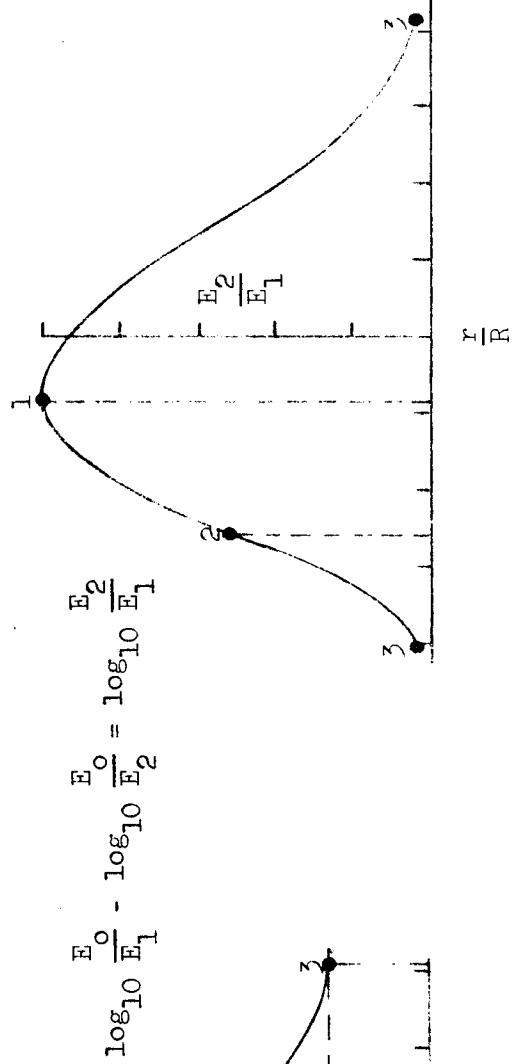
(a) Film calibration



(c) Trace across gas-cap image



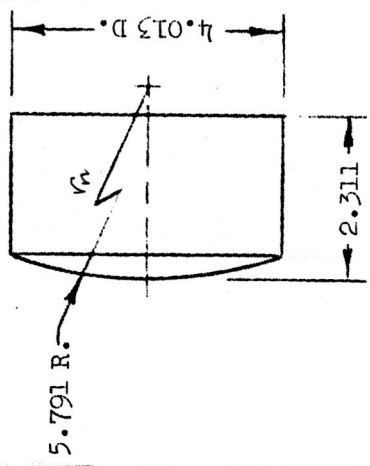
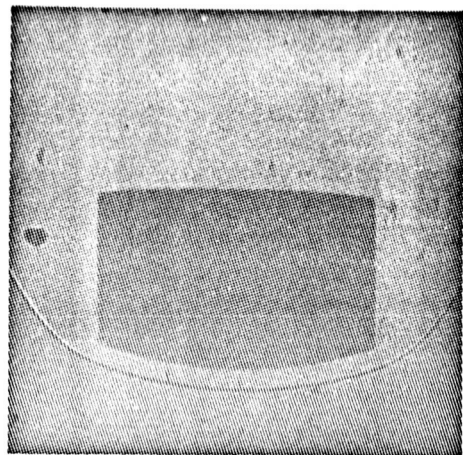
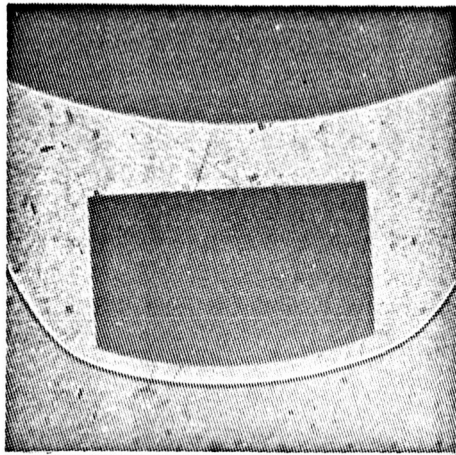
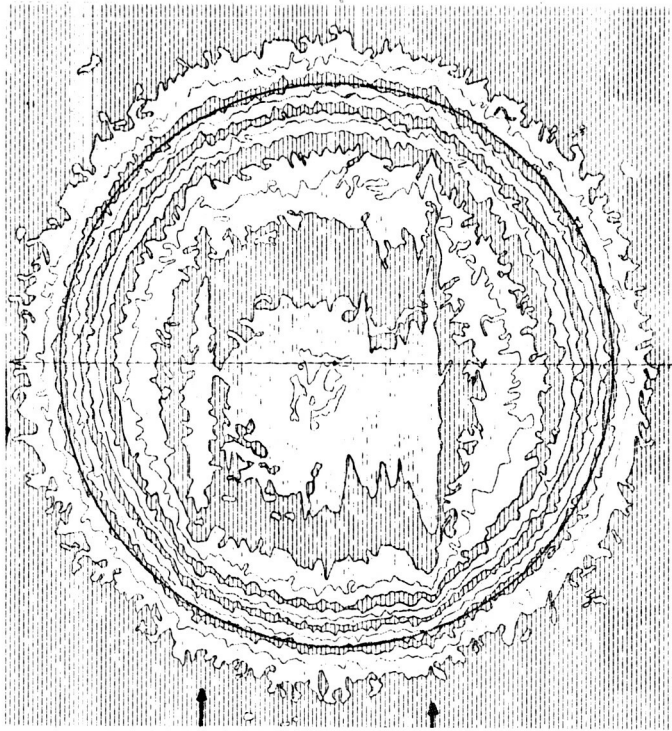
(b) Hurter-Driffield curve.



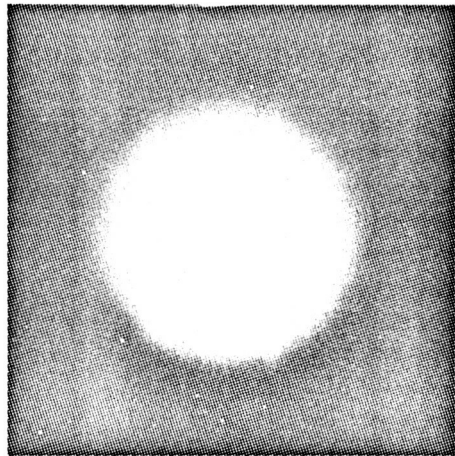
(d) Relative exposure.

Figure 4.- Procedure for determining relative exposures from measured film densities.

$V_{\infty} = 6.48 \text{ km/sec}$      $\alpha = -1.0^{\circ}$   
 $P_{\infty} = 10 \text{ torr}$          $\beta = -3.5^{\circ}$



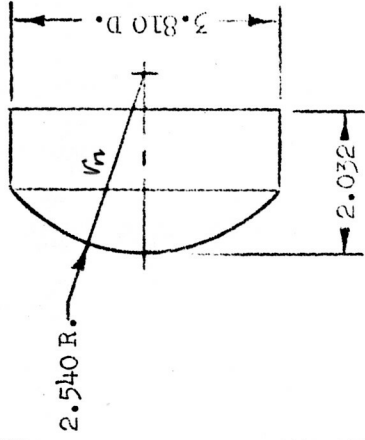
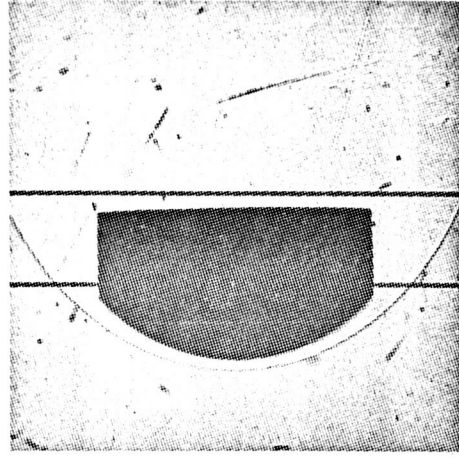
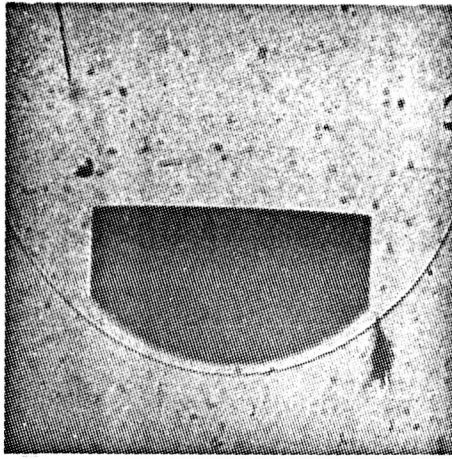
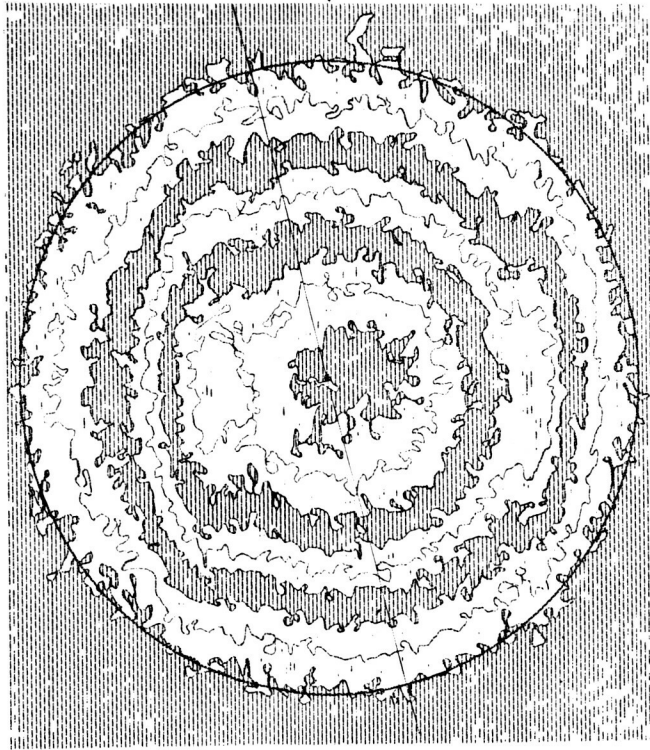
Dimensions in cm



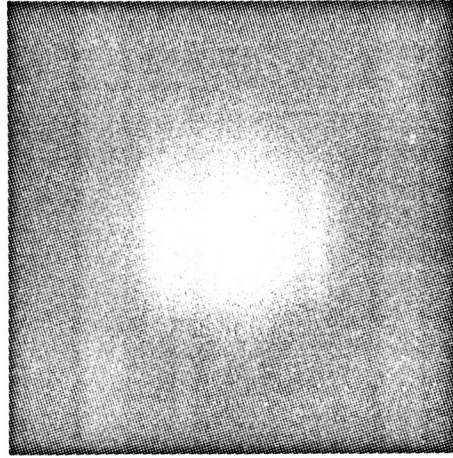
(a)  $\frac{r_n}{D} = 1.44$

Figure 5.- Shadowgraphs, image-converter camera pictures, and Isodensitytraces for spherical-nosed models. 50% CO<sub>2</sub> - 50% N<sub>2</sub> mixture.

$V_{\infty} = 6.80 \text{ km/sec}$   
 $\alpha = -1.3^{\circ}$   
 $P_{\infty} = 5 \text{ torr}$   
 $\beta = 1.6^{\circ}$

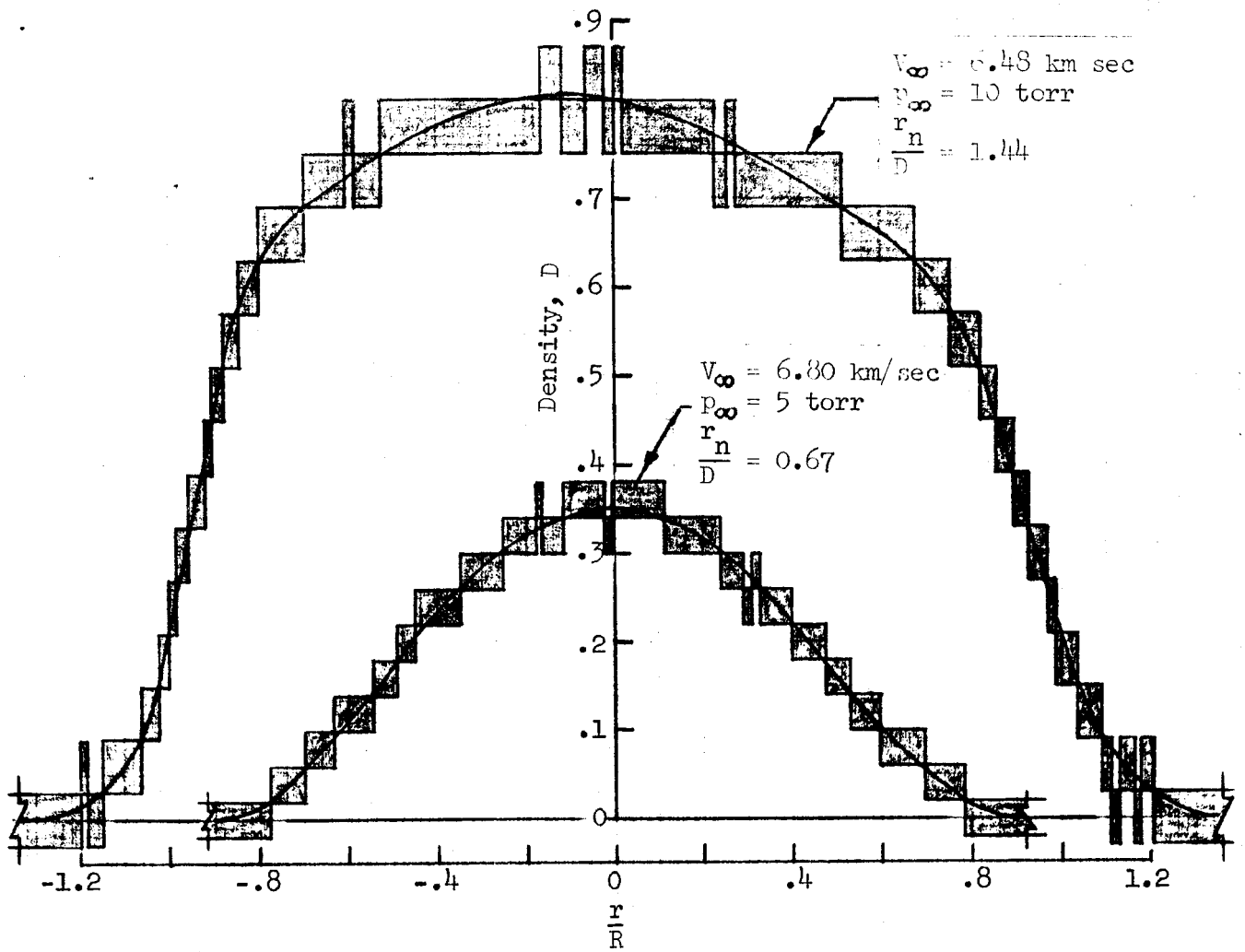


Dimensions in cm

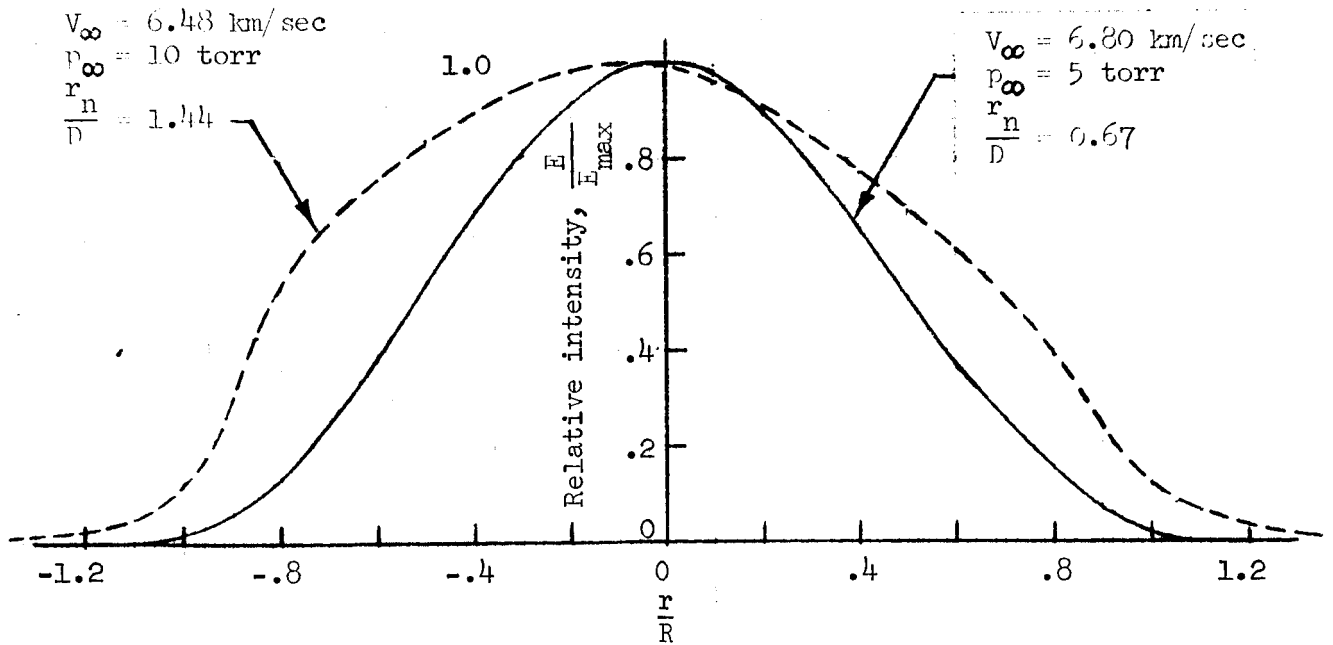


(b)  $\frac{r_n}{D} = 0.67$

Figure 5.- Concluded.

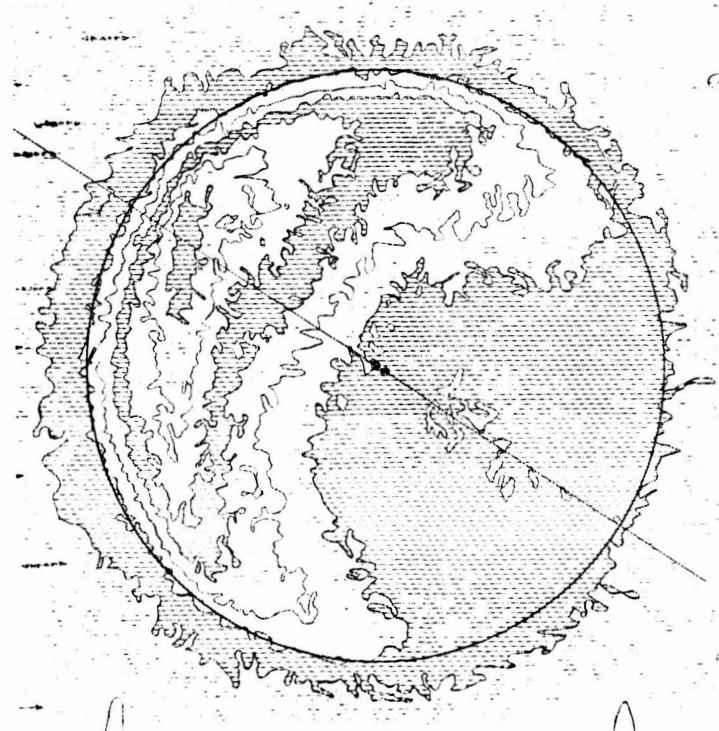
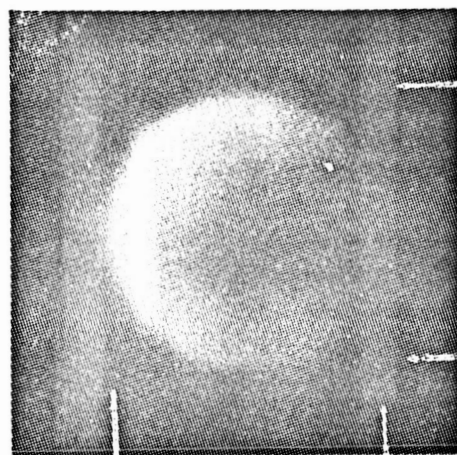
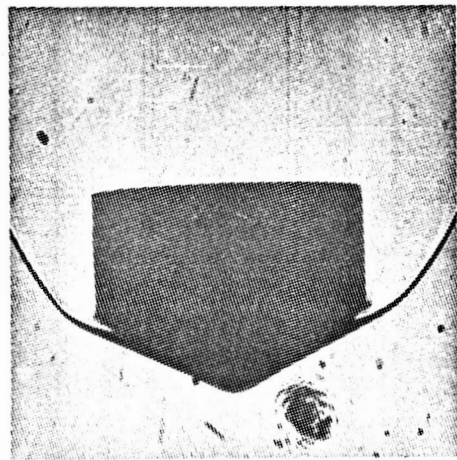
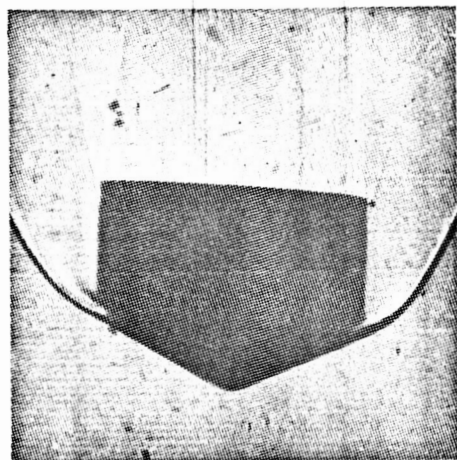
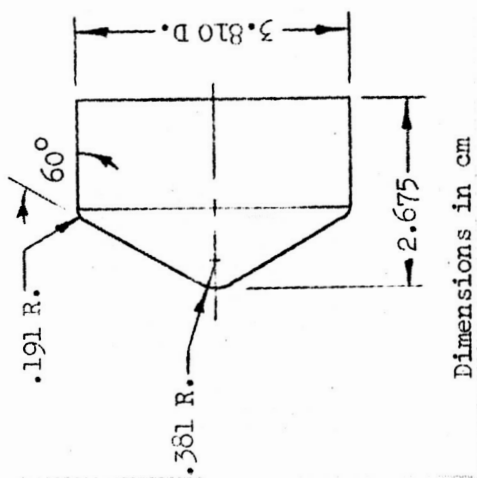


(a) Film density distribution.



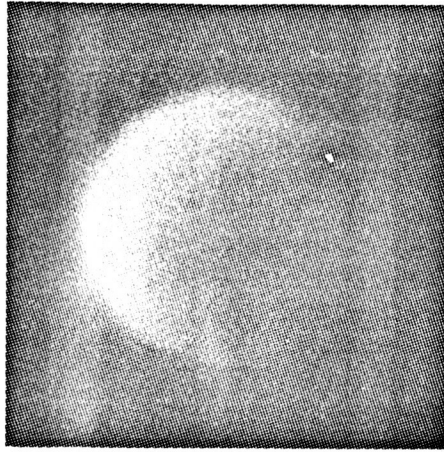
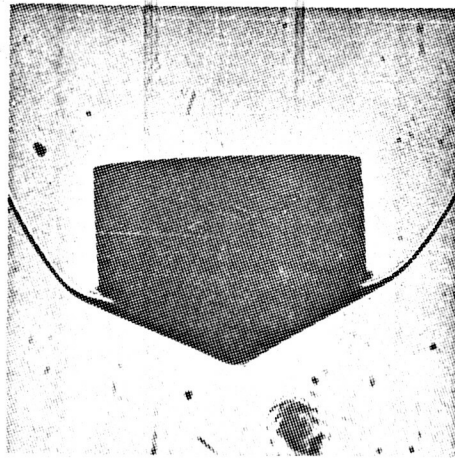
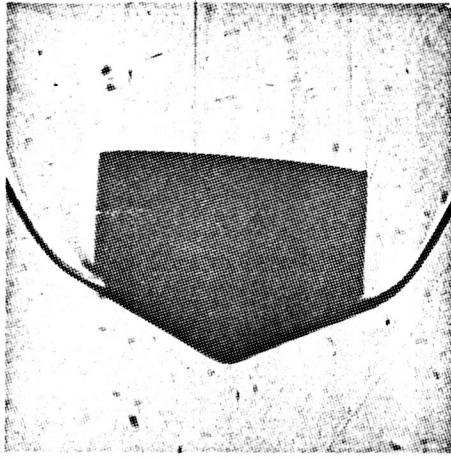
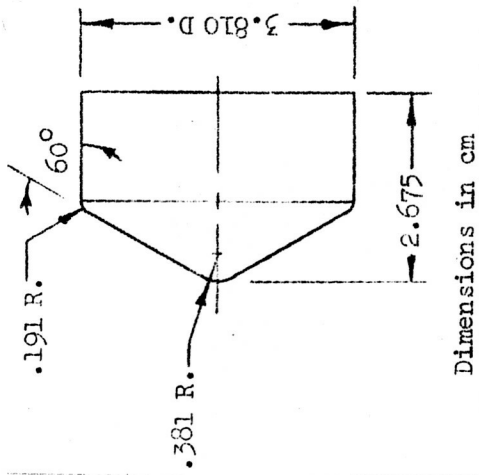
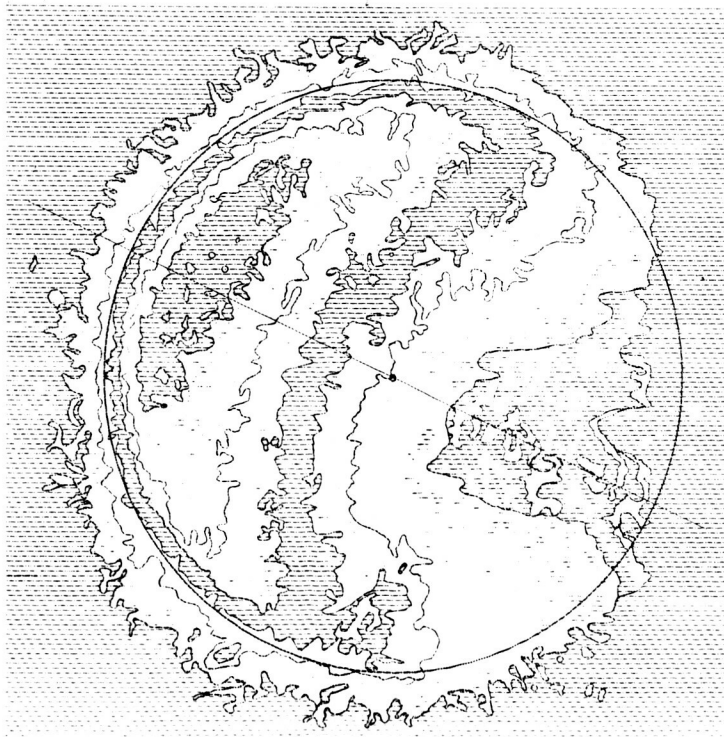
(b) Radiant intensity distribution.

Figure 6.- Film density and radiant intensity distributions for spherical-nosed models. 50%  $\text{CO}_2$  - 50%  $\text{N}_2$  mixture.



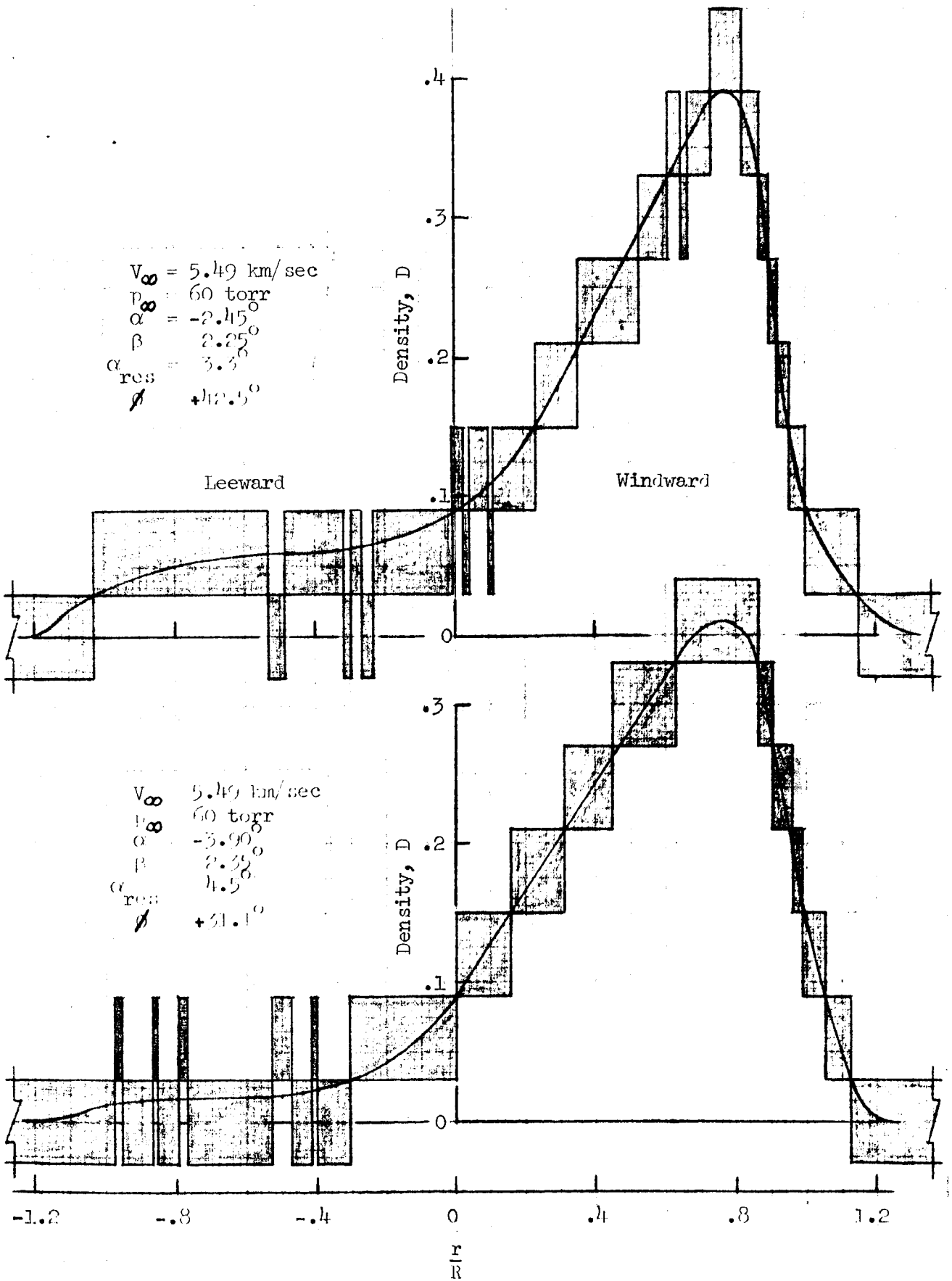
(a)  $\alpha = -2.45^\circ$ ,  $\beta = 2.25^\circ$

Figure 7.- Shadowgraphs, image-converter camera pictures, and Isodensitraces for blunted-cone model.  $V_\infty = 5.49 \text{ km/sec}$  in 50%  $\text{CO}_2$  - 50%  $\text{N}_2$  mixture.



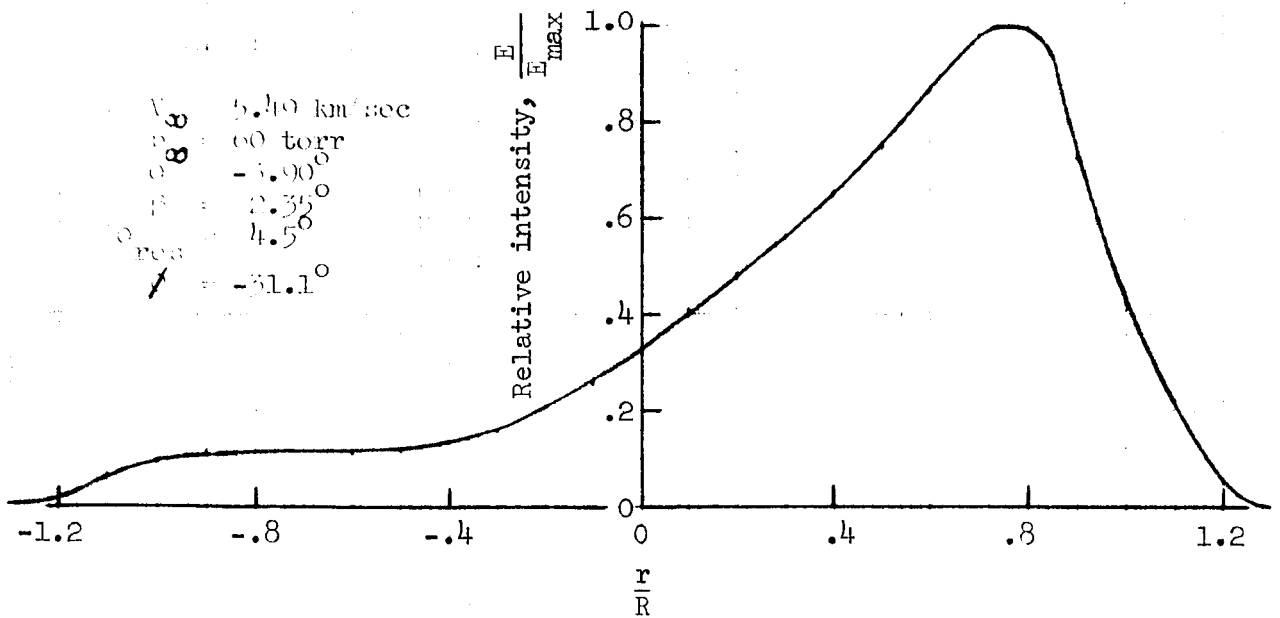
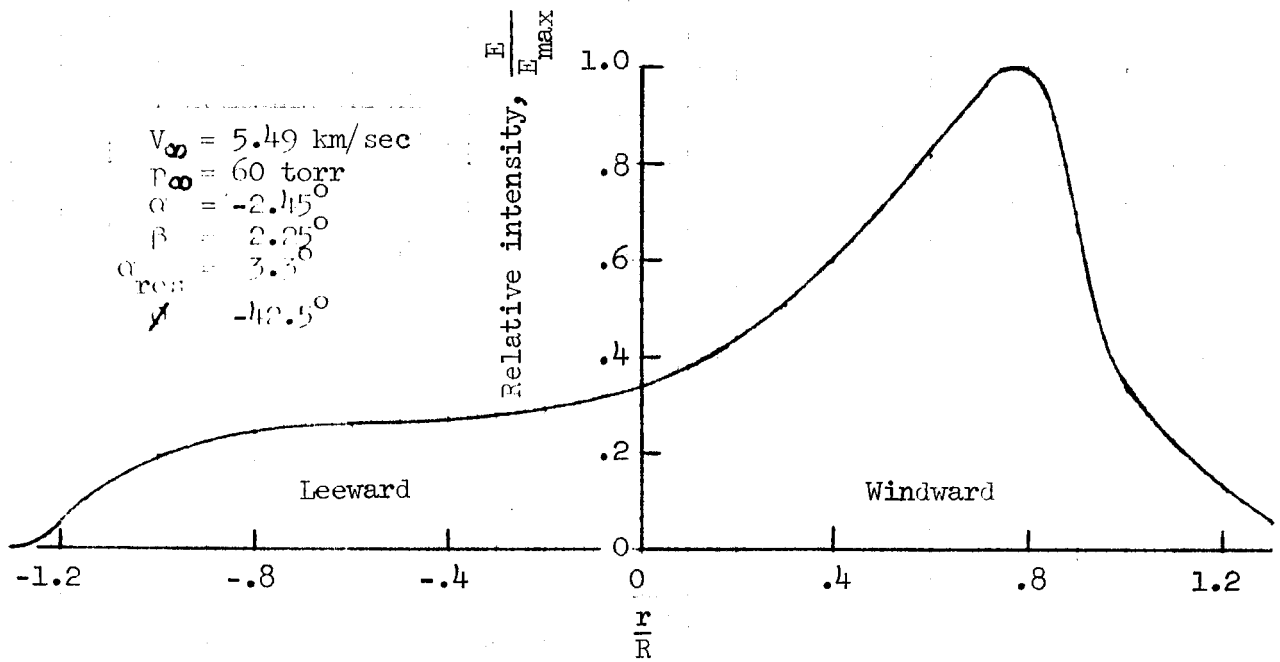
(b)  $\alpha = -3.90^\circ$ ,  $\beta = 2.35^\circ$

Figure 7.- Concluded.



(a) Film density distributions.

Figure 8.- Film density and radiant intensity distributions for blunted-cone model at small angles of attack. 50%  $\text{CO}_2$  - 50%  $\text{N}_2$  mixture.



(b) Radiant intensity distributions.

Figure 8.- Concluded.

$V_{\infty} = 5.30 \text{ km/sec}$      $\alpha = 27.9^{\circ}$   
 $p_{\infty} = 60 \text{ torr}$          $\beta = 27.6^{\circ}$

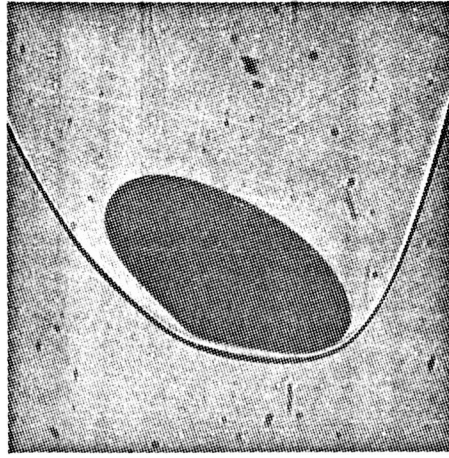
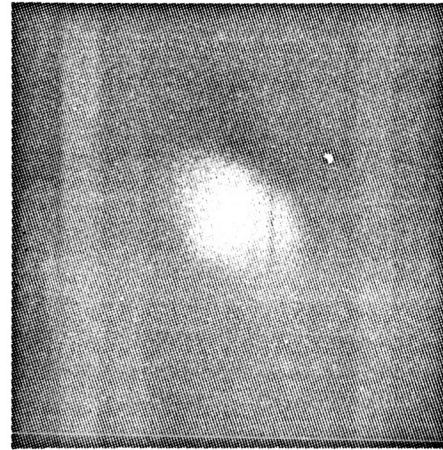
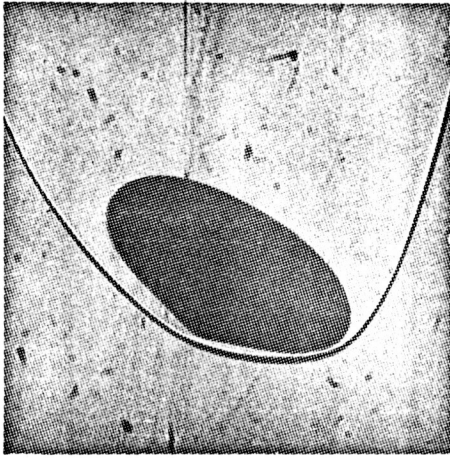
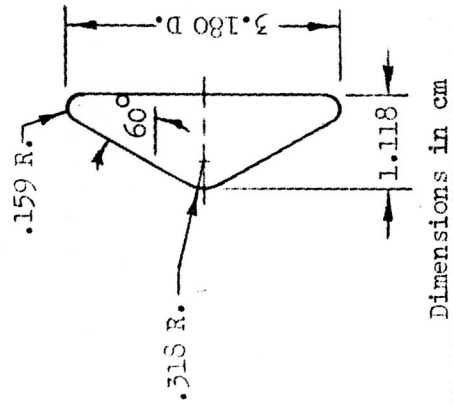
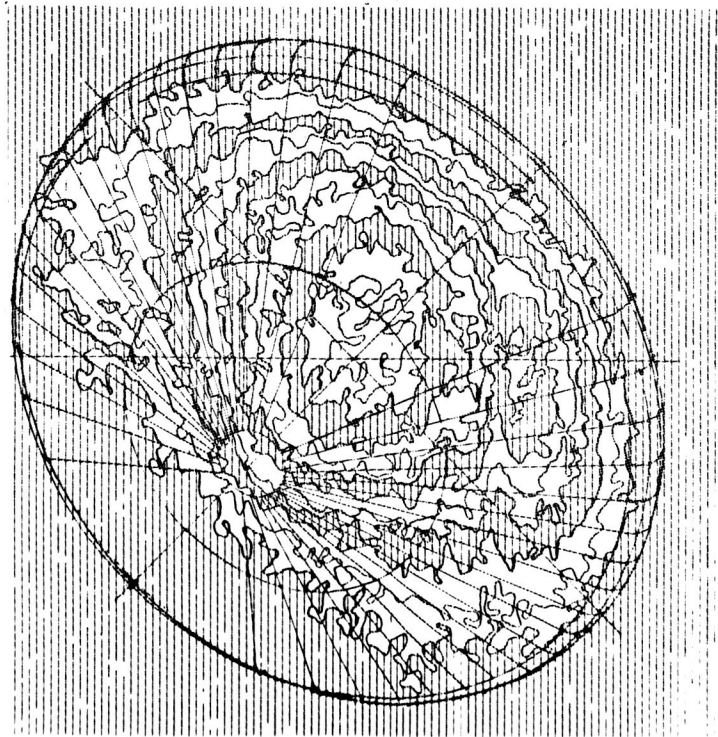
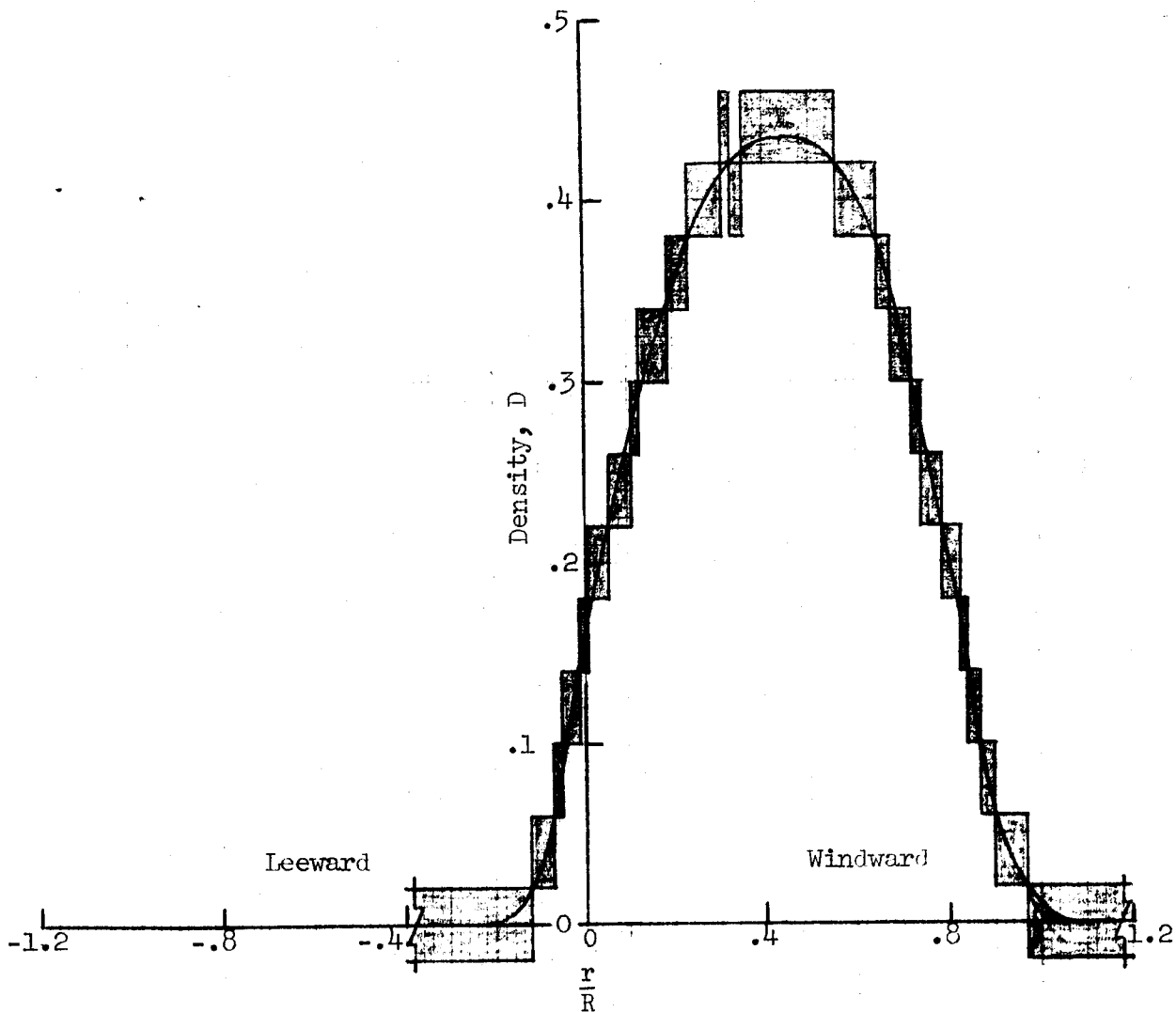
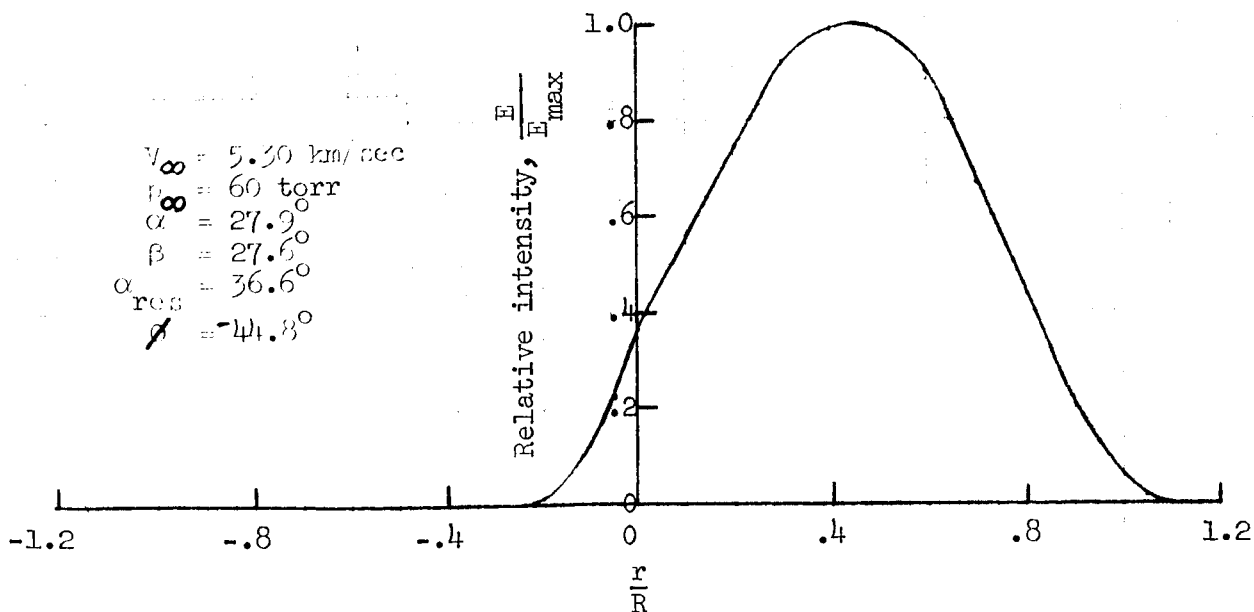


Figure 7.- Shadowgraphs, image-converter camera picture, and Isodensity trace for saboted blunted cone. 50% CO<sub>2</sub> - 50% N<sub>2</sub> mixture.



(a) Film density distribution.



(b) Radiant intensity distribution.

Figure 10.- Film density and radiant intensity along meridian of flow symmetry for blunted-cone model. 50%  $\text{CO}_2$  - 50%  $\text{N}_2$  mixture.